Journal of Materials Science & Technology 92 (2021) 60–68

Contents lists available at ScienceDirect

Journal of Materials Science & Technology

journal homepage: www.elsevier.com/locate/jmst

Research Article

Hard-magnetic liquid metal droplets with excellent magnetic field dependent mobility and elasticity

Xiaokang He, Mingyang Ni, Jianpeng Wu, Shouhu Xuan*, Xinglong Gong*

CAS Key Laboratory of Mechanical Behavior and Design of Materials, Department of Modern Mechanics, CAS Center for Excellence in Complex System Mechanics, University of Science and Technology of China, Hefei 230027, China

ARTICLE INFO

Article history:
Received 26 January 2021
Revised 1 April 2021
Accepted 7 April 2021
Available online 8 May 2021

Keywords:
Magnetic liquid metal droplets
NdFeB particles
Magnetic controllability
Micro-valve

ABSTRACT

Magnetic liquid metal droplets (MLMDs) have been proven to be very important in many fields such as flexible electronics and soft robotics. Usually, soft magnetic particles such as nickel (Ni) and iron (Fe) are mixed or suspended into the liquid metal to obtain soft MLMDs (S-LMDs), which can be easily manipulated under the magnetic field due to the favorable deformability and flexibility. In addition, hard magnetic particles such as neodymium iron boron (NdFeB) with a high residual magnetization can also be dispersed into the liquid metal and the hard MLMDs (H-LMDs) become more compact due to the interaction between internal particles induced by remanence. This work reports a kind of H-LMDs with high surface tension, high flexibility and mechanical robustness, whose electrical conductivity and strength are better than the S-LMDs. Under the magnetic field, the H-LMDs have a faster response time (0.58 s) and a larger actuating velocity (4.45 cm/s) than the S-LMDs. Moreover, the H-LMDs show excellent magnetic controllability, good elasticity and favorable mobility, as demonstrated by magnetically actuated locomotion, bounce tests and rolling angle measurements. Finally, the droplets can be further applied in wheel-driven motors and micro-valve switches, which demonstrates their high application potential in robotic manipulation and microfluidic devices.

1. Introduction

Gallium-based room temperature liquid metal alloys such as Galinstan or EGaIn have received increasing attention due to their diverse and unique properties, including low melting point [1], low evaporation pressure [2], nontoxicity [3], large surface tension [4], high thermal/electrical conductivity [5,6] and superb fluidity [7]. These favorable properties endow gallium-based liquid metal alloys a wide potential applications in flexible electronics and sensors [8–11], stretchable circuits [12–14], soft robotics [15–17] and microfluidics [18,19]. The magnetic manipulation of gallium-based liquid metal alloys is of great significance in these applications. Usually, the manipulation of these liquid metals alloys under an external magnetic field is achieved by modifying their surface or doping with magnetic particles. After being coated or dispersed with magnetic particles, the liquid metal alloys acquire magnetism and become easy to control. The magnetic manipulation provides a favorable actuation for magnetic liquid metals with the advantages of wireless and remote control. For example, the magnetic liquid metals can be manipulated in the microfluidic channel to perform their functions such as electric switches and they can also be designed as motors for drug delivery [20–22].

Magnetic liquid metal droplets (MLMDs) with good elasticity and mechanical robustness can be used to achieve specific functions and it presents a fundamental and promising platform for the application of liquid metals in different fields. Among different kinds of MLMDs, the liquid metal droplets with soft magnetic particles such as Fe and Ni are mostly studied because they are easy to prepare and have good fluidity and deformability [23–25]. Furthermore, Cu doped magnetic liquid metal can be achieved by mixing Fe particles together and the MLMDs show similar appearance, mobility and deformability to the pure liquid metal [26]. Compared with the soft magnetic particles, hard magnetic particles such as NdFeB possessed a large coericivity and unique magnetic polarity reconfigurability. Therefore, the liquid metal droplets with hard magnetic particles can obtain higher surface tension, better elasticity and mechanical robustness due to the interaction of internal magnetic particles caused by remanence. Nonetheless, the research of hard magnetic liquid metal droplets (H-LMDs) still faces some challenges since the lack of a universal method for preparing hard magnetic liquid metal and the hard magnetic particles are easy to be deposited in the liquid metal matrix due to their high density [27,28]. Therefore, developing a simple and versatile method ca-

* Corresponding author.
E-mail addresses: xuansh@ustc.edu.cn (S. Xuan), gongxl@ustc.edu.cn (X. Gong).

https://doi.org/10.1016/j.jmst.2021.04.004
1005-0302/

pable of preparing hard magnetic liquid metal with good dispersion and improving magnetically dependent mechanical properties is highly desired.

In this paper, a versatile method was developed to produce hard magnetic liquid metal with good mobility and deformability. The NdFeB particles were uniformly dispersed in the liquid metal, which endowed the obtained H-LMDs with high surface tension, good mechanical and magnetic properties. The high magnetic controllability, good elasticity and favorable mobility of the H-LMDs were investigated by magnetically actuated experiments, bounce tests, and rolling angle measurements. Comparing with the pure liquid metal droplets (LMDs) and the soft magnetic liquid metal droplets containing Fe particles (S-LMDs), the H-LMDs exhibited better elasticity, mechanical robustness and magnetic maneuverability. Interestingly, the easy manipulation of H-LMDs enabled it to be used as a wheel-driven motor. Finally, by turning on/off of the micro-valve, the H-LMDs showed a wonderful switching applicability in the integrated microfluidic devices.

2. Material and methods

2.1. Materials and chemicals

The Galinstan liquid metal (66.5% gallium, 20.5% indium, and 13% tin) with a melting point of 11 °C was purchased from Yongcheng Co., Ltd., China. Iron (Fe) particles with average diameters of 6 μm and neodymium iron boron (NdFeB) particles with average diameters of 8 and 15 μm were purchased from Sigma-Aldrich. Hydrochloric acid (HCl) was obtained from Sinopharm Chemical Reagent Co., Ltd. NdFeB magnets were purchased from Chizan Co., Ltd., China. Deionized water used in these experiments was self-prepared.

2.2. Preparation of hard magnetic liquid metal

Firstly, the Galinstan liquid metal was squeezed into a clean beaker using a syringe. The surface of the liquid metal was immediately oxidized when exposed in the air, forming an oxide skin. Then the NdFeB particles were added into the beaker and stirred with the Galinstan liquid metal at room temperature for 5 min. After the stirring, the NdFeB particles were fully wrapped by the liquid metal. Next, 1 mol/L HCl solution was added into the beaker to remove the oxide layer on the surface of the liquid metal. In this progress, the direct contact between the HCl solution and the NdFeB particles was avoided since the NdFeB particles were wrapped by the liquid metal, which facilitated the magnetic particles to be well mixed with the liquid metal directly.

2.3. Characterization

The micromorphology of the droplets was observed by scanning electron microscopy (SEM) and related energy-dispersive X-ray spectrum (EDX) (SEM 500, Zeiss, Ltd.). Contact angles were captured by a commercial camera (Nikon, Japan) and extracted by Matlab software. The rolling angles were measured employing a stage with an adjustable tilt angle (Ganwei Metal Products Co., Ltd., China). The images of the droplets were captured via the microscopy and high-speed video camera (Nikon, Japan). The magnetic flux density was measured using a HT20 handheld digital tesla meter (Hengtong Magnetoelectric Technology Co., Ltd., China). The hysteresis loops of the droplets were tested by Hysteresis Measurement of Soft and Hard Magnetic Materials (HyMDC Metis, Leuven, Belgium). The rheological properties of the magnetic liquid metal were carried out by a commercial rheometer (Physica, MCR 302, Anton Paar Co., Austria). The conductivity of the samples were measured by the four wires method through Keithley 2450 source measuring unit (SMU).

3. Results and discussion

3.1. Preparation of the MLMDs

The preparation process of the magnetic liquid metal was shown in Fig. 1a. The liquid metal and the NdFeB particles with a mass ratio of 9:1 were first added into the beaker and stirred at room temperature. Then 1 mol/L HCl solution was added to remove the oxide layer on the surface of the liquid metal. During the preparation progress, this method could effectively avoid the chemical corrosion of the NdFeB particles by HCl solution. For comparison, the magnetic liquid metal with Fe particles were prepared by the common method (stirring Fe particles liquid metal mixture directly in HCl solution). The maximum magnetic particles content in the liquid metal was controlled at 10 wt% to insure the fluidity of the liquid metal [29]. The hard magnetic liquid metal droplets with small-sized NdFeB particles (H-LMD) and large-sized NdFeB particles (H-LMD1) were extruded by a pipette. The pure liquid metal droplet (LMD) and the soft magnetic liquid metal droplet with Fe particles (S-LMD) were also prepared.

Optical images of the droplets mentioned above are shown in Fig. 1c and the volume of them is 8 μL. The images showed that the H-LMD, S-LMD and LMD with a smooth surface well maintained the spherical shape, while the H-LMD1 had an ellipsoidal shape and a rough surface. This result indicated that the size of the magnetic particles had an effect on the morphology of the droplet. The hysteresis loops of the droplets were measured at room temperature (Fig. 1d). The S-LMD exhibited soft magnetic behavior and its hysteresis loop was smooth. The coercivity (6.8 kA/m) and residual magnetization (0.7 emu/g) of the S-LMD were very small, which must be originated from the soft magnetic Fe particles (Fig. S1). In contrast, for the H-LMD1 and H-LMD, the coercivities were 85.4 and 60.7 kA/m, and the residual magnetizations were 7.7 and 8.8 emu/g, respectively. Due to the addition of NdFeB particles, the hard MLMDs exhibited an obvious hard magnetic behavior. The saturated magnetizations of the three droplets were 16, 12 and 13 emu/g, respectively. The hysteresis loops of LMD had no hysteresis and the saturated magnetization was zero. The characteristics, such as wettability, elasticity, mobility and magnetic control capability of the S-LMD, H-LMD and H-LMD1 were investigated as well. The NdFeB particles dispersed in the H-LMD and H-LMD1 were magnetically saturated through a magnetic field before testing. The properties of the H-LMD, S-LMD and LMD were mainly studied in this paper and the relevant data of H-LMD1 were shown in the Supporting Information.

3.2. Rheological properties and electrical conductivity of magnetic liquid metal

According to SEM images, the small-sized NdFeB particles (Fig. 2a) with an average particle size of 8 μm had relatively regular shapes and uniform sizes, while the large-sized NdFeB particles (Fig. S2a) with average particle size of 15 μm had irregular shapes. The average particle size of spherical Fe particles was 6 μm (Fig. S2b). Although the density of the small-sized NdFeB particles (7.8 g/cm^3) was higher than that of the liquid metal matrix (6.48 g/cm^3), the magnetization-enabled high rheological property of the hard magnetic liquid metal (H-LM) could effectively prevent the particle from sedimentation and ensure that the particles were uniformly distributed in the liquid metal matrix (Fig. 2b). The energy dispersive X-Ray spectrometer (EDS) mapping showed there were Ga, In, Sn, Fe and Nd elements in the H-LM (Fig. 2c). For the

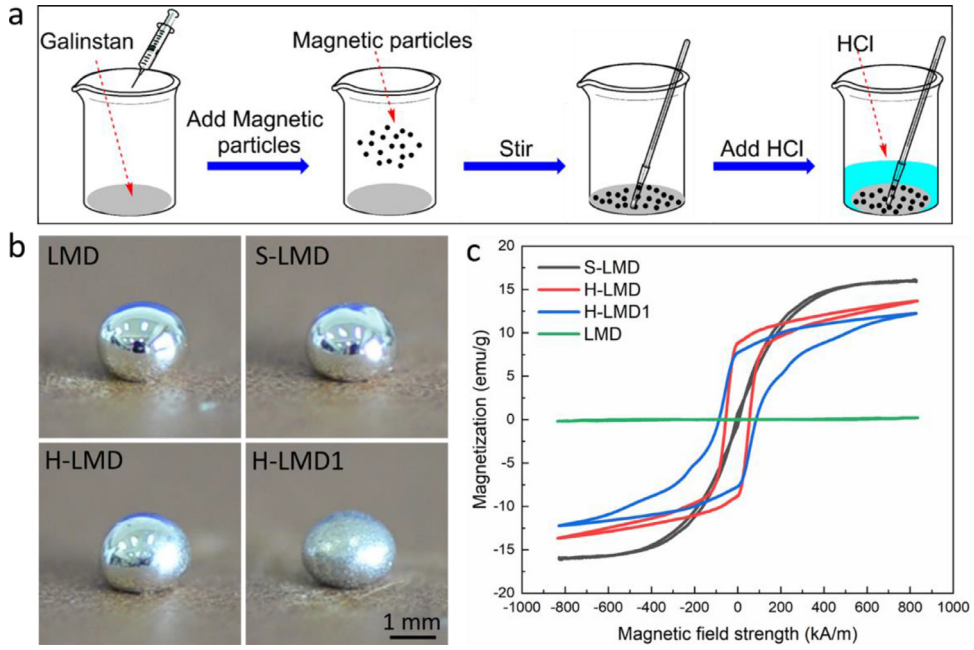

Fig. 1. (a) Schematic diagram of the preparation process of magnetic liquid metal. (b) Optical images of the pure liquid metal droplet (LMD), magnetic liquid metal droplet with Fe particles (S-LMD), large-sized NdFeB particles (H-LMD1) and small-sized NdFeB particles (H-LMD). (c) The magnetic hysteresis loops of the three kinds of MLMDs.

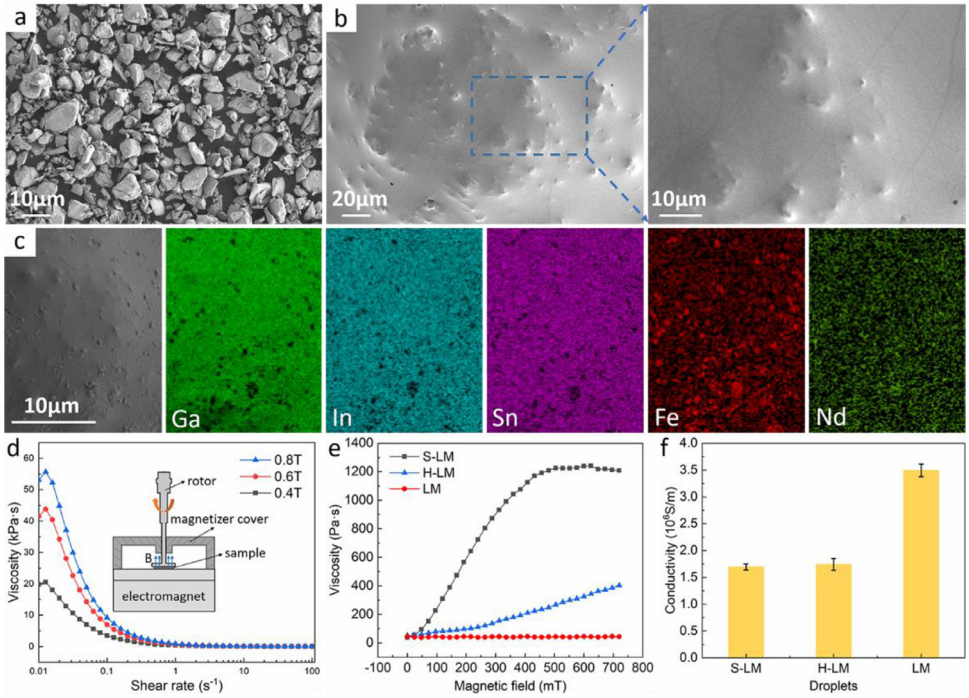

Fig. 2. SEM images of (a) small-sized NdFeB particles and (b) the particles dispersed in the H-LM. (c) EDS mapping of the H-LM. (d) The impacts of shear rates on the viscosity of the H-LM under different magnetic fields. The inset shows schematic illustrations of the Physica MCR302 test system. (e) The impacts of magnetic fields on the viscosity of the three magnetic liquid metal at a constant shear rate of 1 s^{-1}. (f) The electrical conductivity of the S-LM, H-LM and LM.

S-LM, the particles and the matrix were mixed uniformly and there were Ga, In, Sn and Fe elements in it (Figs. S2d and S2e).

Here, rheological properties of the prepared magnetic liquid metal were also explored. The samples were tested at room temperature, the shear rate varied from 0.01 to 100 s^{-1} and the maximum magnetic flux density was 800 mT. The influence of the shear rate on the viscosity of the H-LM under different magnetic flux density was shown in Fig. 2d. It was found that the increased shear rate led to the decrement of the viscosity, indicating that the H-LM exhibited low viscosity under high shear rates. With the increment of magnetic flux density, the initial viscosity of H-LM gradually increased and the maximum initial viscosity was 55 kPa•s. Fig. 2e showed the change of the viscosity for the three kinds of liquid metal with the magnetic field at a shear rate of 1 s^{-1}. The viscosities of the S-LM increased rapidly and then tend to be stable when the magnetic flux density was above 450 mT because the Fe particles inside the S-LM reached magnetic saturation. The viscosity of the H-LM increased with the magnetic field because the in-

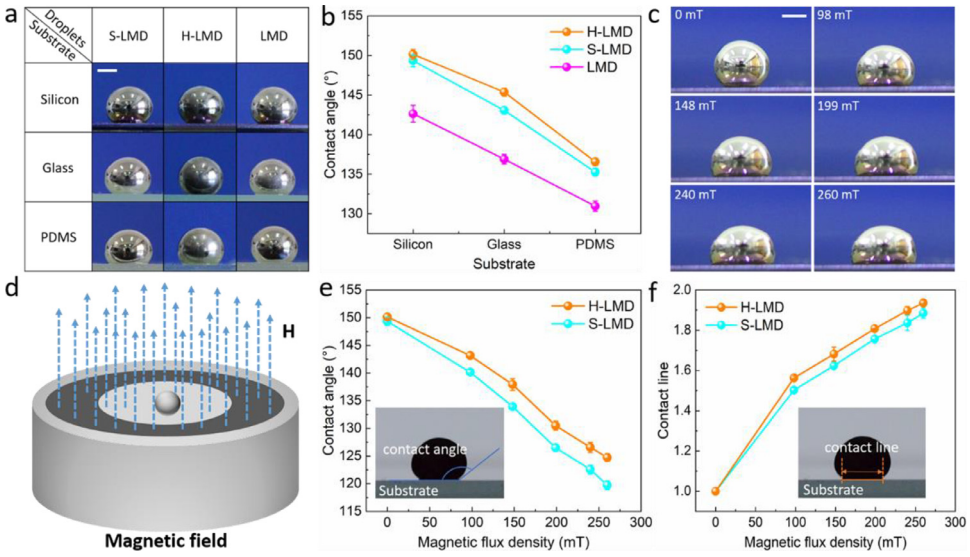

Fig. 3. (a) Images of the contact angle measuring experiment for S-LMD, H-LMD and LMD on silicon wafer, glass, and PDMS substrates. Scale bar =1 mm. (b) The static contact angles of the three kinds of droplets. (c) The changes of droplet morphology under different magnetic flux density. Scale bar =1 mm. (d) Schematic diagram of contact angle test under the magnetic field. (e) The changes of contact angles for H-LMD and S-LMD on silicon substrate under the magnetic field. (f) The changes of contact lines for H-LMD and S-LMD on silicon substrate under the magnetic field.

crement of magnetic field caused more internal molecular friction due to the rapid movement of dispersed NdFeB particles inside the H-LM. The viscosity of the pure liquid metal hardly changed under different shear rates and magnetic fields which proved that the magnetic particles had an effect on the viscosity of the liquid metal [30–32]. Although the NdFeB particles had a low electrical conductivity, the H-LM could achieve an electrical conductivity of about 3.48 $\times$ 10^6 S m^{-1}, which is higher than that of S-LM (Fig. 2f).

3.3. Contact and rolling angle measurements of the droplets

In order to investigate the wettability of the droplets, the contact angle of the H-LMD, S-LMD and LMD were measured on three types of substrates (polydimethylsiloxane (PDMS), glass, and silicon wafer). The wettability of a liquid can be reflected by the static contact angle with the substrate. If the contact angle varies from 0° to 90°, the liquid wets the substrate. Otherwise, the liquid is non-wetting to the substrate. Each droplet (8 μL) was placed on the substrate using a pipette and the static contact angle was measured with the captured droplet's outline. As shown in Fig. 3a, the droplets maintained a spherical shape on all the substrates. The static contact angles of these droplets against different substrates were shown in Fig. 3b. All the contact angles on different substrates were larger than 130°, indicating that the droplets all showed non-wetting properties. The static contact angles of the H-LMD were larger than the other droplets, which were 150.13° $\pm$ 0.61°, 145.37° $\pm$ 0.51°, and 136.57° $\pm$ 0.47° for silicon wafer, glass, and PDMS substrates, respectively. Regardless of the droplets, the static contact angles on the PDMS were the smallest, which attributed to the low surface energy and the chemical inertness [33]. This result also revealed that the surface tension of the H-LMD was higher than that of S-LMD and LMD because the NdFeB particles inside the H-LMD would attract each other due to the presence of remanent magnetism and caused the droplet to be more compact (Fig. S5).

Moreover, the contact angles and contact lines of H-LMD and S-LMD on different substrates were tested under different magnetic flux density. The morphology of the droplet changed due to the movement of the internal magnetic particles under the magnetic field (Fig. 3c). The schematic diagram of the contact angle and contact line measurements under the magnetic field was shown in Fig. 3d. The droplets and the substrate were placed on the electromagnet, and the contact angles and contact lines of the droplets were recorded under different magnetic flux density. As shown in Fig. 3e, the contact angles for the two kinds of droplets gradually decreased with increasing of the magnetic field. The smallest contact angles for H-LMD and S-LMD were 124.73° $\pm$ 0.71°and 119.73° $\pm$ 0.79°, respectively. This is because the magnetic particles inside the droplet were attracted downwards by the electromagnet, resulting in the increase of contact area between the droplet and the substrate thus the contact angle was reduced.

The line formed on the solid-liquid-gas three-phase contact interface when the droplet spreads along the substrate is contact line. Unlike the contact angle, the contact line of the droplet also gradually increased with the contact area between the droplet and the substrate (Fig. 3f). Similar conclusions were obtained on the other two substrates (Fig. S6). The contact angles on PDMS substrate were still the smallest but all the contact angles were larger than 90°, indicating that the droplets were still non-wetting to the substrates under the magnetic field. The large surface tension of the H-LMD improved the stability of the droplets under different magnetic fields and significantly prevented it from deforming. Therefore, the variation range of the contact angle for the H-LMD was smaller than that of S-LMD. This revealed that the addition of NdFeB particles improved the surface tension and the deformation stability of the H-LMD under the magnetic field.

The mobility of the droplets can be evaluated by the critical rolling angle (CRA). The smaller the CRA, the better the mobility. The mobility of the H-LMD, S-LMD and LMD was investigated by testing the CRA on the inclined silicon wafer substrate. The schematic diagram of the rolling angle test is shown in Fig. 4a. Firstly the substrate was glued to the adjustable platform (Fig. 4b), then the droplet was placed on the substrate and the tilt angle was gradually increased until the droplet started to roll. The experiment was repeated five times for each droplet to calculate the average value. As shown in Fig. 4c, the CRAs of the droplets gradually decreased as the size increased. For the same droplet, the larger the volume, the smaller the CRA, indicating that the droplet with larger size had better fluidity. Although the CRAs of H-LMD were

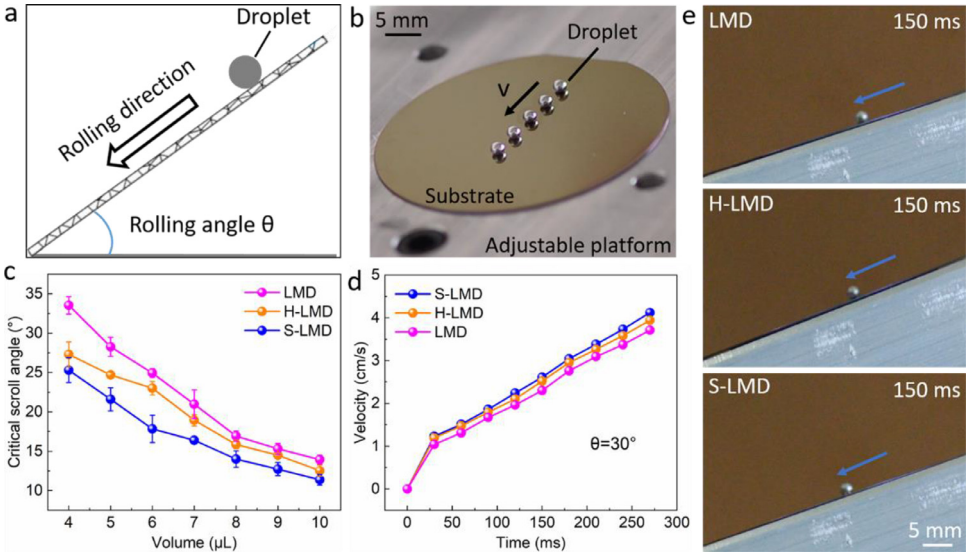

Fig. 4. (a) Schematic diagram of the rolling test on the inclined substrate. (b) Image of the droplet rolling on the platform with an adjustable tilt angle. (c) The critical rolling angles of the LMD, H-LMD and S-LMD with different sizes on the silicon wafer substrate. (d) The rolling velocities of the S-LMD, H-LMD and LMD when rolling at an inclined angle of 30°. (e) Images of the position for the LMD, H-LMD and S-LMD at the same time when rolling from the silicon wafer substrate at an inclination angle of 30°.

slightly larger than that of S-LMD due to the relatively large friction with the substrate, it still had better mobility than the LMD.

Moreover, all the three kinds of droplets (8 μL) could roll down the substrate at an inclined angle of 30° and a distance of 55 mm from the front end. Fig. 4d showed the velocities of the aforementioned droplets (H-LMD, S-LMD and LMD) vs time on the silicon wafer substrate. The velocities of the H-LMD and S-LMD were larger than that of LMD, indicating that the addition of magnetic particles increased the rolling speed of the droplet on the inclined surface. The magnetic particles with uniform sizes have regular shapes and the droplets containing these particles can maintain a spherical shape. Therefore, the friction can be significantly decreased upon rolling. Although the CRAs of H-LMD were slightly larger than the S-LMD, its rolling velocities were similar to that of S-LMD. The H-LMD and S-LMD had a better mobility performance than LMD because the internal magnetic particles were favored for the droplet to maintain a spherical shape, so the friction force decreased when rolling from the substrate. The speed difference of the droplets can be expressed by the position of the droplets on the substrate at the same time. As shown in Fig. 4e, the rolling distance of H-LMD and S-LMD were larger than that of LMD, and the position of them was much closer to the end of the substrate at 150 ms.

3.4. Elasticity and mechanical robustness of the droplets

The elasticity of the H-LMD, S-LMD and LMD was also studied. All the droplets were released from an initial height of 10 cm and impacted on a silicon substrate. The elasticity of different droplets was contrasted by the maximum rebound height, which referred to the maximum height that a droplet bounced after hitting the substrate. A high-speed camera was used to record the rebounding process. A series of images that indicated the positions of the S-LMD, H-LMD and LMD at the corresponding different times were extracted and superposed (Figs. 5a-c). The rebound height of the LMD was 7.9 mm after the first impact (Movie S1). The rebound heights were 9.3 mm and 9.1 mm for the H-LMD and S-LMD after the first impact (Movie S2 and S3). The H-LMD had the highest rebound height because it became more compact due to the addition of NdFeB particles. During each impact, the kinetic energy E_k was quickly converted into surface energy through the deformation of the droplets. Afterwards, the high surface tension drove the droplets back to a spherical shape and the stored surface energy was converted back to E_k again. Meanwhile, some of the energy was lost mainly due to the viscous dissipation during the impact, which scaled as [34]:

$$E_{vis} = \sqrt{\eta \rho_0 R^4 \xi {V_0}^3} \quad (1)$$

where η and ρ_0 is the viscosity and density of the droplet, R is the droplet radius, V_0 is the velocity and ξ denotes the droplet deformation which is highly related to surface tension. In comparison to the S-LMD and LMD, the surface tension of the H-LMD was much higher, which necessitated a much smaller surface deformation ξ upon impact from the same initial height. As a result, the H-LMD lost less E_k and got a higher rebound height. The difference in elasticity could be compared more obviously in Fig. 5d, which summarized the tracks of bouncing tests for the three kinds of droplets. Obviously, the H-LMD showed the best elasticity as it had a higher rebound height compared with the other two droplets.

Fig. 5e showed the changes of the rebound height after the first impact when the droplets fell from different initial heights. Because the droplets obtained more kinetic energy when falling from a higher initial height, the rebound height of the droplet gradually increased with increasing of the initial height. Moreover, the critical height h_0 of all the droplets was larger than 10 cm, which defined as the maximum release height that caused the droplet to bounce. Apart from the good elasticity, the H-LMD was also highly robust, showing a good resisting capability to compression and impact. The mechanical robustness of the S-LMD, H-LMD and LMD was characterized by the critical height h_0 during an impact experiment. As shown in Fig. 5f, when the initial release height h was smaller than h_0, the droplet rebounded and still maintained its original shape. Otherwise, the droplet got damaged following the impact and stuck to the substrate. Depending on the kind of liquid metal droplet, two regimes of behaviors were characterized when h was higher than h_0. The three kinds of droplets were released from a height of 15 cm and their responses after impact were observed through a high-speed camera. As shown in Fig. 5f1, the H-LMD bounced up after impacting the substrate and the integrity of the droplets was maintained. After the first impact, the

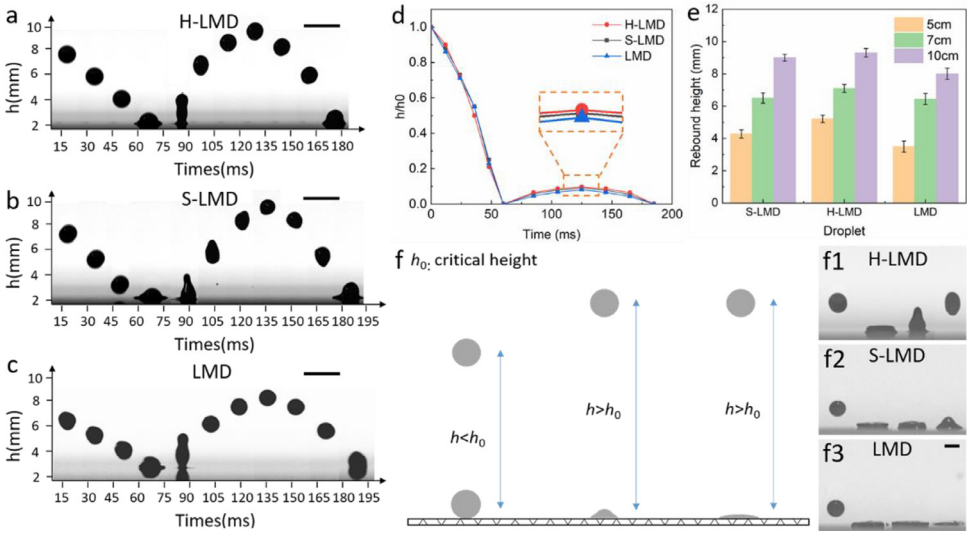

Fig. 5. (a-c) High-speed images demonstrating different behavior of the H-LMD, S-LMD and LMD after impacting the substrate from a height of 10 cm. Scale bar = 5 mm. (d) Bouncing tracks of the three different types of droplets. (e) The rebound height of S-LMD, H-LMD and LMD falling from different heights on the silicon substrate. (f) Scheme of fatal jump of liquid metal droplets. High speed images demonstrating different regimes of the three kinds of droplets upon impacting on the substrate from different heights. Scale bar = 2 mm.

S-LMD had a large deformation and then it stuck to the substrate, maintaining a convex shape (Fig. 5f2). The LMD also stuck to the substrate and completely lost its spherical shape after impacting the substrate (Fig. 5f3). This phenomenon meant that the critical height of the H-LMD was larger than that of S-LMD and LMD because of the good elasticity and high surface tension, revealing it had a better mechanical robustness than the other two droplets.

3.5. Magnetically controllable movability of the droplets

Unlike the LMD, the H-LMD and S-LMD can be controllably manipulated by a magnetic field. To quantify the magnetic controllability of the H-LMD and S-LMD, the max actuating distance l_0 and the average actuating velocity v_0 of the droplets were investigated. The max actuating distance was the maximum distance between the droplet and the magnet when the droplet started to move, and the average actuating velocity was the average speed of the droplet during the movement. Here, the droplets with different sizes were sequentially placed in a petri dish filled with 1 mol/L HCl solution. Then, a magnet was placed under the petri dish to slowly approach the droplet (Fig. 6a). The droplet experienced a magnetic force and moved towards the magnet, in which the position of the droplet was recorded by a ruler. The force analysis of a droplet moving in the petri dish was showed in Fig. 6b. When the droplet moved in HCl solution, it was mainly subjected to the magnetic driving force F_m of the magnet [35],

$$F_m = \frac{V\chi}{\mu_0(1+\chi)}(B\cdot\nabla)B \tag{2}$$

where V is the volume of the droplet, χ is the magnetic susceptibility of the droplet, μ_0 is the magnetic permeability of the free space, and B denotes the magnetic flux density applied on the droplet. For a droplet moving in the petri dish filled with HCl solution, the hydrodynamic drag force can be obtained with the Stokes law,

$$F_h = 6\pi\eta_0 R v \tag{3}$$

where R denotes the radius of the droplet, η_0 is the viscosity of the HCl solution, and v is the velocity of the droplet. In addition, the frictional force between the droplet and the substrate can be formulated as,

$$F_f = \mu mg \tag{4}$$

where m denotes the mass of the droplet, g denotes the gravitational acceleration, and μ is the friction factor. The capillary force induced by the deformation of the droplet can be neglected because the size of the droplet is small and it hardly deforms during movement. So the dynamics of the droplet can thus be formulated as,

$$m\ddot{q} = F_m - F_h - F_f \tag{5}$$

where $\ddot{q}$ denotes the acceleration of the droplet. The relationship between the sizes of the droplets and the measured l_0 was shown in Fig. 6c. For H-LMD and S-LMD, the l_0 of the droplet gradually decreased as the size increased because the droplet with larger size contained more magnetic particles and it was easier to be attracted by the magnetic field. The l_0 of H-LMD was the largest, which meant that it had stronger magnetism and better magnetic properties than the S-LMD.

Fig. 6d presented the magnetic flux density at different distances from the magnet. The maximum value was 220 mT when the Tesla meter was nearby the magnet and decreased to zero once the distance reached 20 mm. The values of magnetic flux density simulated by COMSOL 4.4 (COMSOL Inc., USA) were almost consistent with the testing results. The magnetic lines of induction and the distribution of magnetic flux density around the magnet were shown in Fig. 6e. Obviously, the magnetic field at the edge of the magnet was the strongest. Next, the average actuating velocity v_0 of the droplets with different sizes under an external magnetic field was also tested. Fig. 6f showed the calculated v_0 of the H-LMD and S-LMD with respect to their sizes. Since the droplets with larger sizes could induce a larger hydrodynamic drag F_h and friction F_f when moving in the Petri dish. The resistance force F_h and F_f may increase faster than the magnetic driving force F_m so the velocities of the droplets decreased as the size increased. The highest average actuating velocities for the H-LMD and S-LMD were 4.45 cm/s and 4.08 cm/s when the size was 4 μL. The H-LMD had larger actuating velocity, which indicated that it had better magnetic controllability than the S-LMD.

Additionally, the actuating delay time and the offset distance of the H-LMD and S-LMD were also measured. For the measurement, the magnet was placed underneath the glass substrate and the testing droplet was located directly above the magnet (Fig. 7a). The actuating delay time was defined as the time interval between

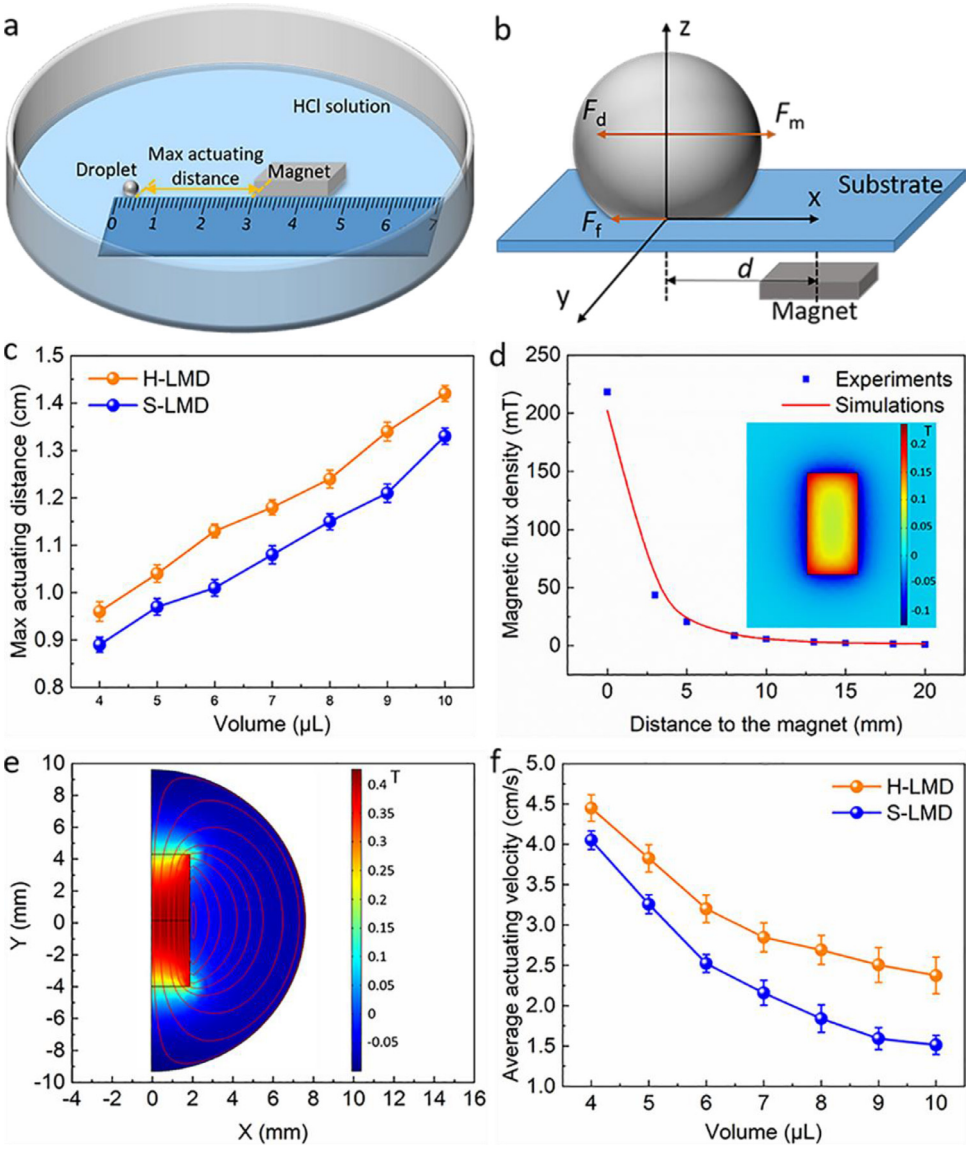

Fig. 6. (a) Magnetic controllability testing system. (b) Schematic of force analysis for a droplet moving on the glass substrate. (c) The relationship between the sizes of the droplets and the max actuating distance. (d) The magnetic flux density versus to the distance away from the magnet surface. (e) Distribution of magnetic lines of induction around the magnet. (f) The relationship between the sizes of the droplets and the average actuating velocity.

the movement of the magnet and the droplet. The start times of the magnet and the testing droplet were noted as t_0 and t_1, respectively, and the delay time was calculated by $t_1 - t_0$. In Fig. 7b, the actuating delay time for the H-LMD and S-LMD were 0.58 s and 0.83 s respectively. In addition, the offset distance *d*, defined as the distance from the center of the droplet to the center of the magnet when the droplet started to move, could also be used to describe and quantify the magnetic controllability of the two droplets. The S-LMD had an offset distance of 5.94 mm, while it was 5.27 mm for the H-LMD (Fig. 7b). The H-LMD had smaller actuating delay time and shorter offset distance than the S-LMD because of the strong magnetism and it was easier to be attracted by magnets, showing the high sensitivity and low time delay under the magnetic field.

It is noteworthy that the droplet is always at the edge of the magnet when following the magnet movement during the testing process because the magnetic field at the edge of the magnet is the largest according to Fig. 6d. The static friction force and the resistance moment caused by the deformation of the droplet hindered the movement of the droplet. In order to overcome the resistance moment, a longer offset distance was required to drive the droplet to roll [36]. Due to the small actuating delay time and the short offset distance, the H-LMD was used as the driving motor for wheeled robots (Fig. 7d). A double nozzle high precision 3D printer (Flashforge, ltd., China) was utilized to print the wheel model with a diameter of 3 cm and the H-LMD (8 μL) was placed at the bottom of the wheel inside (Fig. 7c). A magnet was used to actuate the H-LMD, which changed the center of gravity for the wheel and caused the wheel to roll forward (Movie S4). The entire moving process was untethered, which meant that the H-LMD exhibited promising revolutionary uses and good magnetic maneuverability.

3.6. Application of the droplets in a micro-valve

Based on the above study, the H-LMD was magnetically controllable with a better elasticity and mechanical robustness than the S-LMD. These properties enabled it to be applied in the integrated microfluidic devices, such as micro-valve [37,38]. In this work, a liquid metal droplet-based micro-valve was designed and fabricated to demonstrate the practical use of the H-LMD under

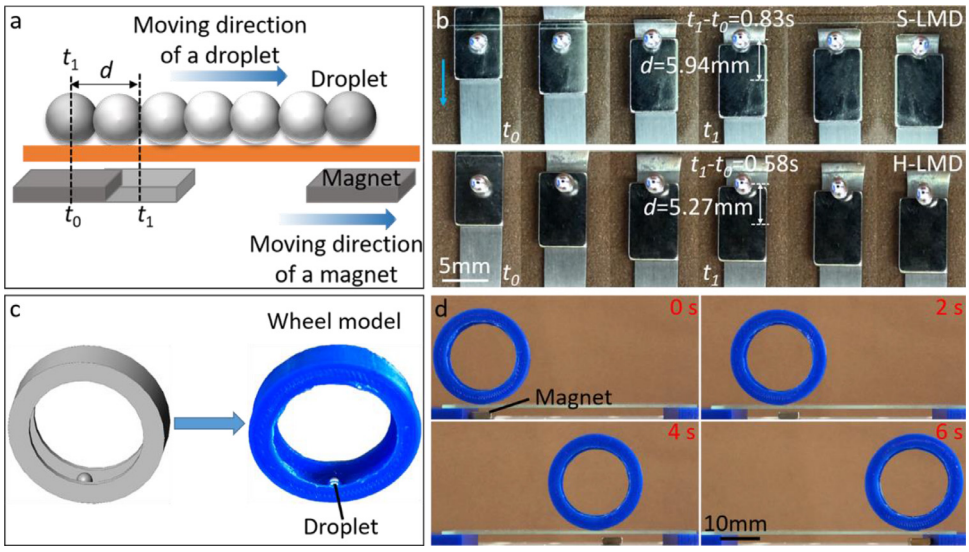

Fig. 7. (a) Schematic diagram of the actuating delay time experiment. (b) High-speed images from the movement of the magnet to the movement of S-LMD and H-LMD. (c) Schematic diagram of the wheel model. (d) Actuating process of the wheel. The wheel was placed on a glass substrate and actuated by a magnet.

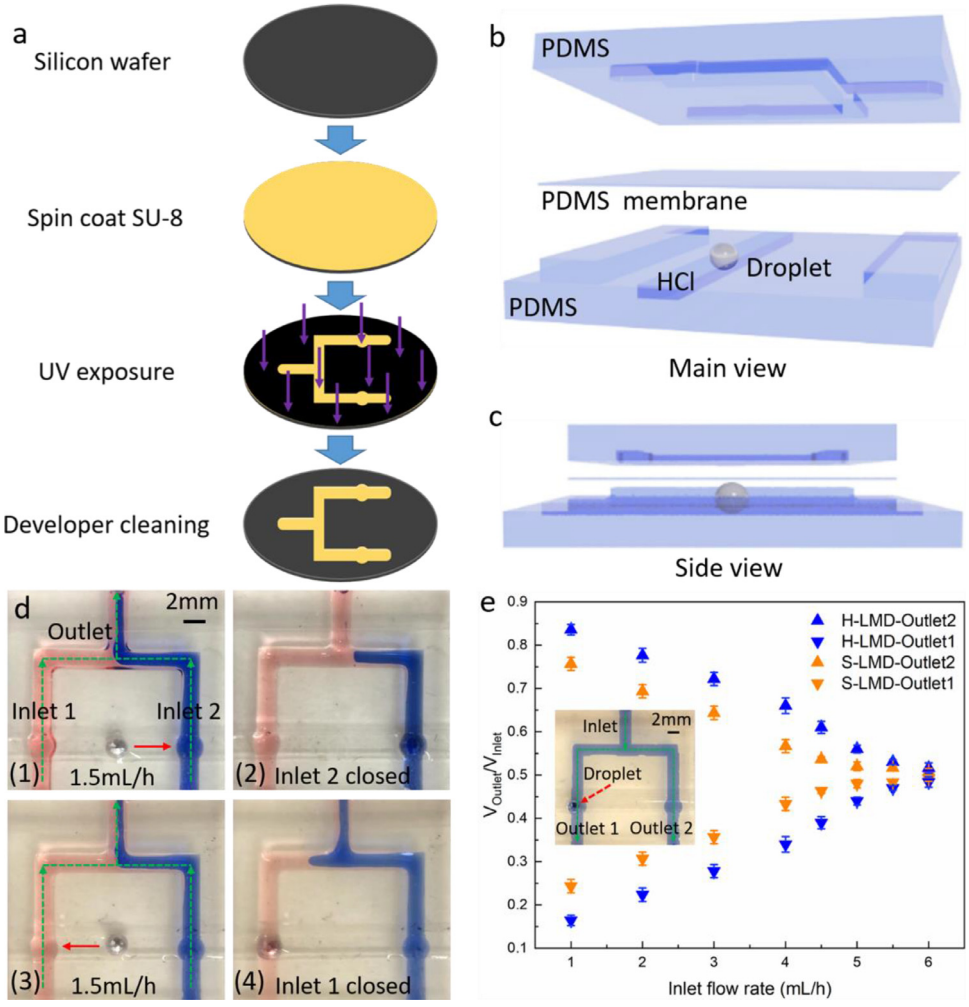

Fig. 8. (a) Schematic diagram of the fabrication of the microfluidic chip used in fabricating micro-valve. (b-c) Structure of the liquid metal droplet-based micro-valve. (d) The open and close process of the micro-valve by manipulation of the H-LMD with an applied magnetic field. (e) Comparison of the efficiency for the micro-valve when the inlet flow rate is changed from 1 mL/h to 6 mL/h.

the magnetic field. The microfluidic chip was used to fabricate the microfluidic channel in the micro-valve, which was made by the soft lithography technique. The fabrication process of the microfluidic chip was shown in Fig. 8a. The micro-valve consisted of three parts: the top PDMS layer with a microfluidic channel, a PDMS membrane and the bottom PDMS layer for the droplet to move (Figs. 8b and 8c). The thickness of the top and bottom PDMS layers were 3 mm and the size of the channel in the bottom PDMS layer was 20 mm × 3 mm × 1 mm. In order to facilitate the manufacture, the thickness of the PDMS membrane was chosen as 50 μm. Water and mineral oil were used in the micro-valve, the water was dyed blue and the mineral oil was dyed red for easy observation.

Fig. 8d showed the open and close process of the micro-valve by manipulating the H-LMD under the magnetic field. At the beginning, the micro-valve was opened and the two fluids could easily pass through the microfluidic channel. When the droplet moved under the thin PDMS membrane (as the bottom part of the microfluidic channel), it pressed the PDMS membrane. The interaction between the droplet and the PDMS membrane was shown in Fig. S8. The PDMS membrane deformed under the squeeze of the droplet and the flow rate of the liquid on this side gradually slowed down. The liquid in the channel on the other side gradually occupied the outlet port, then the micro-valve was closed (Movie S5 and S6). Two high accurate syringe pumps (LSP02–1B, LongerPump) were used to pump the water and mineral oil into the microfluidic channel from the inlet port. The efficiency of the micro-valve was shown in Fig. 8e. In general, the efficiency decreased when the inlet flow rate increased. Compared with the S-LMD, the micro-valve controlled by H-LMD had higher efficiency, which revealed that the H-LMD exhibited great potential in microfluidic fields.

4. Conclusion

In summary, a hard magnetic liquid metal droplets (H-LMDs) was reported by homogenously dispersing NdFeB particles into the liquid metal matrix, which increased the surface tension of the droplet and improved its magnetic and mechanical properties. The properties of H-LMDs were tested by contact and rolling angle measurements, bounce tests and magnetically actuated locomotion. Compared with the S-LMDs and LMDs, the H-LMDs showed favorable mobility, good elasticity and mechanical robustness. In addition, the H-LMDs had a shorter actuating delay time of 0.58 s and a larger actuating velocity of 4.45 cm/s than the S-LMDs under the magnetic field, showing good magnetic sensitivity and magnetic control stability. Finally, the capabilities of H-LMDs as a wheel-driven motor and a switch for the micro-valve were also demonstrated owing to their excellent controllability and good magnetic maneuverability, which expanded the applicability of liquid metal in robotic manipulation and microfluidic devices.

Declaration of Competing Interest

The authors declare that they have no known competing financial interests or personal relationships that could have appeared to influence the work reported in this paper.

Acknowledgments

Financial support from the National Natural Science Foundation of China (Grant Nos. 11822209, 12072338, 11772320), the Fundamental Research Funds for the Central Universities (WK2480000007), Joint Fund of USTC–National Synchrotron Radiation Laboratory (KY2090000055), and the Strategic Priority Research Program of the Chinese Academy of Sciences (Grant No. XDB22040502) are gratefully acknowledged. Thanks to the instrumentation support from engineering practice center of USTC.

Supplementary materials

Supplementary material associated with this article can be found, in the online version, at doi:10.1016/j.jmst.2021.04.004.

References

[1] H.J. Koo, J.H. So, M.D. Dickey, O.D. Velev, Adv. Mater. 23 (2011) 3559–3564.
[2] M.R. Khan, C. Trlica, J.H. So, M. Valeri, M.D. Dickey, ACS Appl. Mater. Interfaces 6 (2014) 22467–22473.
[3] T.Y. Liu, P. Sen, C. Kim, J. Microelectromech. Syst. 21 (2012) 443–450.
[4] S.Y. Tang, B. Ayan, N. Nama, Y.S. Bian, J.P. Lata, X.S. Guo, T.J. Huang, Small 12 (2016) 3861–3869.
[5] H.Y. Li, J. Liu, Front. Energy 5 (2011) 20–42.
[6] M.G. Kim, H. Alrowais, S. Pavlidis, O. Brand, Adv. Funct. Mater. 27 (2017) 1604466.
[7] C. Jin, J. Zhang, X.K. Li, X.Y. Yang, J.J. Li, J. Liu, Sci. Rep. 3 (2013) 3442.
[8] S. Zhu, J.H. So, R. Mays, S. Desai, W.R. Barnes, B. Pourdeyhimi, M.D. Dickey, Adv. Funct. Mater. 23 (2013) 2308–2314.
[9] Y. Mao, Y. Wu, P. Zhang, Y. Yu, Z. He, Q. Wang, J. Mater. Sci. Technol. 61 (2021) 132–137.
[10] C.B. Cooper, K. Arutselvan, Y. Liu, D. Armstrong, Y.L. Lin, M.R. Khan, J. Genzer, M.D. Dickey, Adv. Funct. Mater. 27 (2017) 1605630.
[11] K. Luo, T. Huang, Y. Luo, H. Wang, C. Sang, X. Li, J. Mater. Sci. Technol. 29 (2013) 401–405.
[12] C.F. Pan, K. Kumar, J.Z. Li, E.J. Markvicka, P.R. Herman, C. Majidi, Adv. Mater. 30 (2018) 1706937.
[13] Q. Wang, Y. Yu, J. Yang, J. Liu, Adv. Mater. 27 (2015) 7109–7116.
[14] H. Zuo, H. Li, L. Qi, S. Zhong, J. Mater. Sci. Technol. 32 (2016) 485–488.
[15] J. Zhang, Y.Y. Yao, L. Sheng, J. Liu, Adv. Mater. 27 (2015) 2648–2655.
[16] J. Wu, S.Y. Tang, T. Fang, W.H. Li, X.P. Li, S.W. Zhang, Adv. Mater. 30 (2018) 1805039.
[17] Y.Y. Yao, J. Liu, RSC Adv. 6 (2016) 56482–56488.
[18] S.Y. Tang, K. Khoshmanesh, V. Sivan, P. Petersen, A.P. O'Mullane, D. Abbott, A. Mitchell, K. Kalantar-zadeh, Proc. Nat. Acad. Sci. U.S.A. 111 (2014) 3304–3309.
[19] L.W. Hao, J.D. Liu, Q. Li, R.K. Qing, Y.Y. He, J.Z. Guo, G. Li, L.L. Zhu, C. Xu, S. Chen, J. Mater. Sci. Technol. 83 (2021) 203–211.
[20] J. Jeon, J.B. Lee, S.K. Chung, D. Kim, Lab Chip 17 (2017) 128–133.
[21] J. Guo, F. Zeng, J. Guo, X. Ma, J. Mater. Sci. Technol. 37 (2020) 96–103.
[22] J. Zhang, R. Guo, J. Liu, J. Mater. Chem. B 4 (2016) 5349–5357.
[23] X.P. Li, S. Li, Y.M. Lu, M.Z. Liu, F.X. Li, H. Yang, S.Y. Tang, S.W. Zhang, W.H. Li, L.N. Sun, ACS Appl. Mater. Interfaces 12 (2020) 37670–37679.
[24] B. Ma, C.T. Xu, J.J. Chi, J. Chen, C. Zhao, H. Liu, Adv. Funct. Mater. 29 (2019) 1901370.
[25] L. Hu, H.Z. Wang, X.F. Wang, X. Liu, J.R. Guo, J. Liu, ACS Appl. Mater. Interfaces 11 (2019) 8685–8692.
[26] F.X. Li, S.L. Kuang, X.P. Li, J. Shu, W.H. Li, S.Y. Tang, S.W. Zhang, Adv. Mater. Technol. 4 (2019) 1800694.
[27] L.X. Cao, D.H. Yu, Z.S. Xia, H.Y. Wan, C.K. Liu, T. Yin, Z.Z. He, Adv. Mater. 32 (2020) 2000827.
[28] Y. Li, Z.J. Qi, J.X. Yang, M.X. Zhou, X. Zhang, W. Ling, Y.Y. Zhang, Z.Y. Wu, H.J. Wang, B.A. Ning, H. Xu, W.X. Huo, X. Huang, Adv. Funct. Mater. 29 (2019) 1904977.
[29] L. Ren, S.S. Sun, G. Casillas-Garcia, M. Nancarrow, G. Peleckis, M. Turdy, K.R. Du, X. Xu, W.H. Li, L. Jiang, S.X. Dou, Y. Du, Adv. Mater. 30 (2018) 1802595.
[30] C.C. Yang, Z. Liu, M.C. Yu, X.F. Bian, J. Mater. Sci. 55 (2020) 13303–13313.
[31] M.C. Yu, X.F. Bian, T.Q. Wang, J.Z. Wang, Soft Matter 13 (2017) 6340–6348.
[32] T. Jiemsakul, S. Manakasettharn, S. Kanharattanachai, Y. Wanna, S. Wangsuya, S. Pratontep, J. Magn. Magn. Mater. 422 (2017) 434–439.
[33] D. Kim, D. Jung, J.H. Yoo, Y. Lee, W. Choi, G.S. Lee, K. Yoo, J.B. Lee, J. Micromech. Microeng. 24 (2014) 055018.
[34] P. Aussillous, D. Quere, Proc. R. Soc. A 462 (2006) 973–999.
[35] M.A. Bijarchi, A. Favakeh, E. Sedighi, M.B. Shafii, Sens. Actuators A Phys. 301 (2020) 111753.
[36] R. Chen, Q. Xiong, R.Z. Song, K.L. Li, Y.X. Zhang, C. Fang, J.L. Guo, Adv. Mater. Interfaces 6 (2019) 1901057.
[37] G.Y. Li, J.K. Du, A.B. Zhang, D.W. Lee, J. Appl. Phys. 126 (2019) 084505.
[38] M.Q. Li, D.Q. Li, Anal. Chim. Acta 1021 (2018) 85–94.